Rare Met. (2023) 42(7):2250–2260
https://doi.org/10.1007/s12598-022-02257-x

RARE METALS

ORIGINAL ARTICLE

Functional layer engineering to improve performance of protonic ceramic fuel cells

Ning Wang, Zhi-Yin Huang, Chun-Mei Tang, Li-Xin Xing, Ling Meng, Yoshitaka Aoki*, Lei Du*, Si-Yu Ye

Received: 15 September 2022 / Revised: 30 October 2022 / Accepted: 30 October 2022 / Published online: 4 May 2023

Abstract Protonic ceramic fuel cells (PCFCs) have been attracting increasing attention because of their advances in high-efficiency power generation in an intermediate-temperature range, as compared to the high-temperature solid oxide fuel cells (SOFCs). The greatest difference between PCFCs and SOFCs is the specific requirement of protonic (H^+) conductivity at the PCFC cathode, in addition to the electronic (e^-) and oxide-ion (O^{2-}) conductivity. The development of a triple $H^+/e^-/O^{2-}$ conductor for PCFC cathode is still challenging. Thus, the most-widely used cathode material is based on the mature e^-/O^{2-} conductor. However, this leads to insufficient triple phase boundary (TPB), i.e., reaction area. Herein, an efficient strategy that uses a ~ 100 nm-thick proton conductive functional layer ($La_{0.5}Sr_{0.5}CoO_{3-\delta}$, LSC55) in-between the typical $La_{0.8}Sr_{0.2}CoO_{3-\delta}$ cathode (a mature e^-/O^{2-} conductor, LSC82) and $BaZr_{0.4}Ce_{0.4}Y_{0.1}Yb_{0.1}O_{3-\delta}$ electrolyte (11 mm in diameter, 20 μm in thickness) is proposed to significantly enhance the reaction area. Reasonably, the ohmic resistance and polarization resistance are both decreased by 47% and 62%, respectively, compared with that of PCFCs without the functional layer. The power density of the PCFC with such a functional layer can be raised by up to 2.24 times, superior to those described in previous reports. The enhanced PCFC performances are attributed to the well-built TPB and enhanced reaction area via the functional layer engineering strategy.

Keywords Protonic ceramic fuel cell (PCFC); Cathode functional layer (CFL); Power density; Triple phase boundary (TPB)

1 Introduction

With the optimization of the global energy structure, it is extremely urgent to develop and utilize clean energy, e.g., hydrogen. Solid oxide fuel cells (SOFCs) at high temperature (typically 800−1000 °C) have gained much attention as a high-efficiency technology to convert hydrogen into electrical energy [1, 2]. Although the high working temperature improves the high energy efficiency, the harsh conditions usually lead to short lifetime and high maintaining cost of SOFCs. Alternatively, the protonic ceramic fuel cells (PCFCs) have recently emerged. PCFCs work is based on protonic conducting electrolyte, other than the SOFCs based on oxide-ion (O^{2-}) conducting electrolyte. Because the activation energy for proton conduction is 0.3−0.6 eV, which is much lower than that for O^{2-} conduction (~ 0.8 eV), PCFCs can function below 700 °C. In this regard, PCFCs are a promising device to utilize clean hydrogen energy [3–7].

Developing high-performance PCFCs that operates at a relatively low temperature is particularly desired, e.g., at 600 °C [8–10]. However, two obstacles at decreased working temperature must be considered: one is the high

N. Wang, Z.-Y. Huang, L.-X. Xing, L. Meng, L. Du*, S.-Y. Ye
Huangpu Hydrogen Energy Innovation Center, School of Chemistry and Chemical Engineering, Guangzhou University, Guangzhou 510006, China
e-mail: lei.du@gzhu.edu.cn

N. Wang, C.-M. Tang
Graduate School of Chemical Sciences and Engineering, Hokkaido University, Sapporo 060-8628, Japan

Y. Aoki*
Faculty of Engineering, Hokkaido University, Sapporo 060-8628, Japan
e-mail: y-aoki@eng.hokudai.ac.jp

ohmic resistance (R_o) of the electrolyte and the other is high polarization resistance (R_p) of the cathode. Great efforts have been devoted to decreasing R_o by using a thinner electrolyte. For example, by decreasing the thickness of the $BaZr_{0.1}Ce_{0.7}Y_{0.2}O_{3-\delta}$ electrolyte from 18 to 10 μm, the R_o can be decreased from 0.66 to 0.24 $\Omega\cdot cm^2$ at 500 °C [11, 12]. Other works suggest that the R_o can be optimized to 0.1–0.15 $\Omega\cdot cm^2$ if the electrolyte thickness can be controlled at ~2.5 μm [13, 14]. However, controlling the electrolyte to be thin is challenging in terms of both the electrolyte production and PCFC fabrication. Exploring advanced strategies to decrease R_o is thus attractive [5].

On the other hand, it is essential to decrease R_p is to facilitate the kinetics at cathode side. The design and synthesis of cathode materials have been thus intensively investigated. So far, oxides with double O^{2-}/e^- conductivities, such as $La_{0.6}Sr_{0.4}Co_{0.2}Fe_{0.8}O_{3-\delta}$ (LSCF), $Ba_{0.5}Sr_{0.5}Co_{0.2}Fe_{0.8}O_{3-\delta}$ (BSCF), and $La_{0.8}Sr_{0.2}CoO_{3-\delta}$ (LSC82) [15, 16], have been widely used as the cathodes in PCFCs, because these types of oxides are well-understood in the field of SOFCs. However, as previously mentioned, the protonic conductivity is important in a PCFC cathode. Otherwise, protons from the electrolyte cannot transfer across the cathode, leading to fewer cathode−electrolyte−gas triple phase boundaries (TPBs), a low reaction area and low kinetics. Accordingly, the non-existence or insufficiency of proton conductivity in these double oxides demonstrates high R_p (> 0.4 $\Omega\cdot cm^2$) at the temperature below 600 °C [3, 15, 16]. An effective solution to address this issue is to develop oxides with simultaneous triple $H^+/O^{2-}/e^-$ conductivity [17–24]. However, the development of a triple $H^+/O^{2-}/e^-$ conductor is at its preliminary stage because the proton conductivity in oxides is still limited by the insufficient hydration reaction, e.g., $> 1 \times 10^{-5}$ $S\cdot cm^{-1}$ is required to active the electrode [5, 8, 25–27].

Herein, a strategy based on a cathode functional layer (CFL) with triple conductivity is proposed to decrease both R_o and R_p. Significantly, this is accomplished without employing a thinner electrolyte or triple $H^+/O^{2-}/e^-$ conducting cathode. Specifically, a thin $La_{0.5}Sr_{0.5}CoO_{3-\delta}$ (LSC55) layer is fabricated in-between the conventional $BaZr_{0.4}Ce_{0.4}Y_{0.1}Zr_{0.1}O_{3-\delta}$ (BZCYYb) electrolyte and $La_{0.8}Sr_{0.2}CoO_{3-\delta}$ (LSC82) cathode. Because of the significantly decreased R_o and R_p, the output power density of a PCFC cell is remarkably improved by 2.24 times compared with that without this functional layer. Moreover, this study investigated the mechanisms for the extended reaction area and enhanced performance. The results demonstrated the potential of this functional layer engineering strategy for developing advanced PCFCs.

2 Experimental

2.1 Synthesis of LSC82 cathode powder

$La_{0.8}Sr_{0.2}CoO_{3-\delta}$ (LSC82) powder was synthesized using a previously reported citrate precursor method referring to Refs. [28, 29]. Briefly, $La(NO_3)_3\cdot 6H_2O$, $Sr(NO_3)_2$, and $Co(NO_3)_2\cdot 6H_2O$ (high purity chemicals, 99.99%, used without pretreatment) following the required stoichiometry were dissolved in H_2O (Milli-Q). Citric acid (CA; $C_6H_8O_7\cdot H_2O$) was then added as a chelate agent at a mole ratio of CA:LSC82 = 2:1. The obtained solution was heated to 60 °C and maintained for 3 h under vigorously stirring in order to evaporate H_2O and promote polymerization. The obtained gelatinous product was calcinated at 500 °C for 1 h in the air, which yielded a precursor with deep color. Finally, the precursor was annealed at 800 °C for 15 h in pure O_2 in a tube furnace, producing the LSC82 cathode powder.

2.2 Synthesis of electrolyte and anode precursors

$BaCO_3$ (high purity chemicals, 99.95%), ZrO_2 (high purity chemicals, 98%), CeO_2 (high purity chemicals, 99.99%), Y_2O_3 (high purity chemicals, 99.99%), and Yb_2O_3 (high purity chemicals, 99.99%), along with 3.56 wt% of $Zn(NO_3)_2\cdot 6H_2O$ (Wako chemicals, 99.9%) were ball-milled in ethanol for 48 h and subsequently dried at 80 °C to obtain the precursor powder for BZCYYb electrolyte. The BZCYYb electrolyte precursor and NiO were mixed in ethanol at a weight ratio of 40:60 and ball-milled for 48 h to obtain the anode precursor.

2.3 Fabrication of functional layer and PCFCs

A specific amount of anode precursor was uniaxially pressed under 20 MPa and subsequently pressed isostatically under a hydrostatic pressure of 100 MPa. After that, green anode pellets (~ 12 mm in diameter, ~ 1.2 mm in thickness) were obtained. Then, an electrolyte precursor slurry was prepared by dispersing the electrolyte precursor powder into a solution containing a dispersant (20 wt% polyethylenimine (molecular weight (M_w) = 28,000) dissolved in α-terpineol) and binder (5 wt% surfactant dissolved in α-terpineol). The electrolyte precursor slurry was spin-coated on both sides of the anode pellets, followed by co-sintering at 1450 °C for 12 h in an air atmosphere. Accordingly, the compact ceramic disks in ca. Φ 9 mm × 1 mm were obtained. The backs of the ceramic disks were polished with a mechanical grinder to remove the electrolyte. Thus, the anode | electrolyte configuration was obtained.

A functional layer of $La_{0.5}Sr_{0.5}CoO_{3-\delta}$ (LSC55, ~ 100 nm) was coated on the electrolyte side using radio frequency (RF, 40 W) sputtering at 500 °C for 2 h in Ar atmosphere, prior to post annealing at 700 °C for 1 h in O_2 atmosphere. The cathode slurry was prepared by dispersing 2 g LSC82 cathode powder in isopropanol (5 ml), α-terpineol (5 ml), molding aids (1 ml) and ethylene (0.3 g). Then the cathode slurry was coated on the LSC55 functional layer by screen printing, forming a configuration of anode | electrolyte | functional layer | cathode. Pt paste was applied to the anode as a current collector, just as in our previous reports [24, 28]. Finally, the cell was annealed at 700 °C for 1 h in air. As a reference, the cell without the functional layer was also prepared.

2.4 Physical characterization

X-ray powder diffraction (XRD, Rigaku, Ultima IV) was used to evaluate the phase purity using Cu Kα radiation (40 kV, 20 mA) in a 2θ range of 5°–90°. The scan rate and 2θ step were 5 $(°)\cdot min^{-1}$ and 0.02°, respectively. Scanning electron microscopy (SEM) and energy dispersive X-ray spectroscopy (EDX) were performed on a SIGMA500 (ZEISS).

2.5 PCFC performance test

The PCFC cathode was sealed in a glass tube filled with synthetic air (20 vol% O_2 and 80 vol% Ar fed bubbled through water at 30 $ml\cdot min^{-1}$ (H_2O pressure of 2330 Pa)), while humidified H_2 (10 $ml\cdot min^{-1}$) with 3% water was fed into the anode side. The same gas flows were used in electrolysis mode tests. The impedance spectra of the PCFCs were obtained with a Solartron 1260A frequency response analyzer implemented with a Solartron 1287 potentiostat in the frequency range of 10^6–0.1 Hz with an AC amplitude of 30 mV under an open circuit voltage (OCV) condition in a temperature range of 500–700 °C. The current–voltage (*I*–*V*) and current–power (*I*–*P*) characteristics were recorded on the same apparatus.

3 Results and discussion

3.1 Phase structure and microstructure

Figure 1a shows XRD pattern of the $La_{0.8}Sr_{0.2}CoO_{3-\delta}$ (LSC82) cathode powder, which was annealed at 800 °C for 15 h in a pure oxygen atmosphere. The LSC82 powder exhibited a single perovskite structure without the appearance of any second phase. Meanwhile, all the diffraction peaks were identical to those of rhombohedral $La_{0.9}Sr_{0.1}CoO_{3-\delta}$ (PDF No. 28-1229). The microstructural features of the LSC82 powder are shown in Fig. 1b, where the grain size was evenly distributed. The calculated average size based on this SEM image was about 82 nm, which was smaller than those of previously reported cathode materials [30–33]. The small size usually benefits high available surface area. In addition, EDX images shown in Fig. 1c–f suggest that the La, Sr, Co, and O were uniformly distribute in the whole sample. Reasonably, it was desirable to use this LSC82 as the PCFC cathode because it could provide more active sites for the cathodic reaction.

We fabricated PCFCs with and without the CFL in-between the electrolyte and cathode (see the details in Sect. "Experimental"). Figure 2a shows the cross-sectional SEM image of the PCFC with the CFL. It is clearly to observe three distinct layers: the anode BZCYYb + NiO, 20 μm-thick electrolyte BZCYYb (including the LSC55 CFL), and LSC82 cathode from bottom to top. The LSC55 CFL was difficult to be directly observed due to the extremely thin film with the thickness of about 90 nm, which is prepared by the same method with our previous report [34]. SEM image of the electrolyte (Fig. 2b) demonstrates a dense surface while the anode remains good porous structure (Fig. 2c) to provide enough active sites for hydrogen diffusion and reduction. XRD patterns of the anode, electrolyte (BZCYYb) and electrolyte with CFL (BZCYYb + LSC55) are presented in Fig. 2d. The anode exhibits the peaks of NiO and pure perovskite structure. Although the BZCYYb and BZCYYb + LSC55 have the same diffraction features assigned to the pure perovskite structure, the lattice constants are different, as implied from the peak shifts (Fig. 2e and f) for the two cells. The above results suggest that there was no impurity in the anode and electrolyte.

3.2 Electrochemical performances of PCFCs

In order to evaluate the role of the CFL, the electrochemical performances of PCFCs with and without the CFL were tested at the temperature range of 500–700 °C. The obtained *I*–*V* curves are shown in Fig. 3a, b. The evolution of the OCV versus operating temperature based on these two curves is presented in Fig. 3d. By decreasing the operating temperature from 700 to 500 °C, the OCV increased from 0.99 to 1.14 V for the PCFC without the CFL and from 0.99 to 1.11 V for the PCFC with the CFL. The theoretical OCV could be calculated according to the Nernst equation, which changes from 1.14 to 1.16 V at decreasing temperature from 700 to 500 °C. The gap between the theoretical and practical OCV values was attributed to the hole conduction in the BZCYYb electrolyte [24].

On the other hand, the power densities of the PCFCs with the CFL were much higher than those for PCFCs

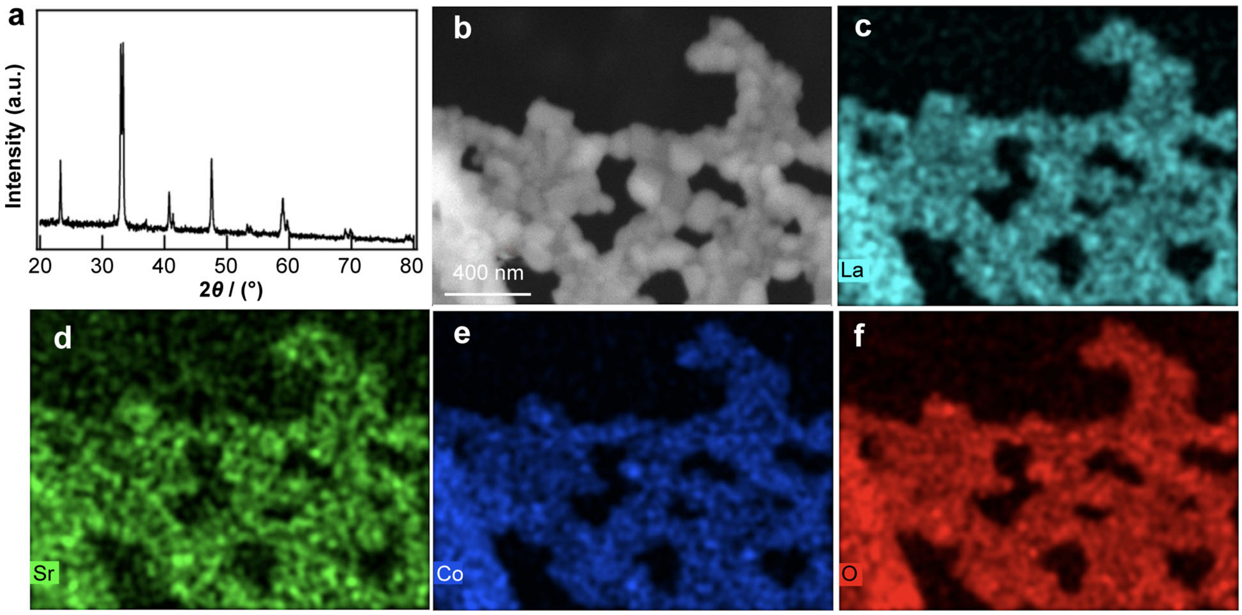

Fig. 1 **a** XRD pattern, **b** SEM image and EDX images of **c** La, **d** Sr, **e** Co, and **f** O for LSC82 powder annealed at 800 °C in O_2 atmosphere for 15 h

without the CFL at specific temperatures (comparing Fig. 3a with Fig. 3b). The changes of peak power densities (PPDs) vs. temperature for different cells are illustrated in Fig. 3c. The PPDs of PCFCs without the CFL were 414, 233, 162, 137 and 80 $mW \cdot cm^{-2}$ at 700, 650, 600, 550 and 500 °C, respectively. These values can be significantly improved to 783, 520, 364, 255 and 159 $mW \cdot cm^{-2}$, respectively, by applying the CFL strategy. What should be emphasized is that the PPD at 600 °C is raised by 2.24 times after introducing CFL. Such an improvement is remarkably better than previous reports [8, 35, 36]. For example, the PPD was increased by 0.37 times by introducing $(Pr,Ba,Sr)(Co,Fe)O_3$ interlayer [8], by 0.8 times when using a BZCYYb1711 layer [35].

We list the published PPD values of typical and recent PCFCs in Table 1 [5, 15, 37–42]. Except for those PCFCs with excellent PPDs [5, 41, 42], most PCFCs using a Zr-rich BZCYYb electrolyte usually exhibited limited power densities, and most of the PPDs were lower than 400 $mW \cdot cm^{-2}$ at 700 °C. The PPD of a PCFC based on a $BaZr_{0.4}Ce_{0.4}Y_{0.2}O_3$ (BZCY442) cathode was 360 $mW \cdot cm^{-2}$ at 700 °C, [37] while that with the renowned $Ba_{0.5}Sr_{0.5}Co_{0.2}Fe_{0.8}O_3$ (BSCF) cathode presents 381 $mW \cdot cm^{-2}$ [15]. This comparison indicates that the PPD (783 $mW \cdot cm^{-2}$) at 700 °C obtained in this study is among the best as compared to those found in the literature.

The electrochemical impedance spectra (EIS) were measured under the OCV condition at 700–500 °C for the PCFCs with and without the CFL. The recorded results and fitting curves are shown in Fig. 4. In general, the x-axis intercept at the high frequency represents the ohmic resistance (R_o) of the cells, which includes the resistance of proton conduction in the electrolyte (main contribution), the contact resistance is associated with the interface, and the electronic resistance of the electrodes. The diameter of the semi arc provides the R_p at the cathode side. It has been widely accepted that the semi arc includes two distinct semi arcs, named as R_1 and R_2. Accordingly, it is reasonable to fit the EIS with an equivalent circuit model with the configuration of R_o–(R_1-CPE$_1$)–(R_2-CPE$_2$) as depicted in the inset of Fig. 4a, where R and CPE represent the resistance and constant phase element (i.e., pseudo-capacitance), respectively. S_1 and S_2 as shown in Fig. 4b are interpreted by the parallel components of (R_1-CPE$_1$) and (R_2-CPE$_2$), respectively [24, 34]. Therefore, R_1 and R_2 provide the polarization resistance related to S_1 and S_2, so that they are renamed as R_{p1} and R_{p2}. The R_{p1} from 1×10^5 to 1×10^2 Hz represents the charge transfer resistance (electrochemical proton incorporation, Reaction (3)), and the R_{p2} from 1×10^5 to 1×10^{-1} Hz usually reflects the resistance of mass transfer on the cathode (the surface diffusion or association desorption of oxygen species on the cathode side, Reactions (1, 2, 4)) during the cathodic reacting process. Accordingly, EIS curves of the PCFC with and without the CFL at different temperatures are fitted, as shown in Fig. 4a–e; meanwhile, the fitted results of R_o (and calculated proton conductivity), R_{p1}, R_{p2} and R_p are plotted against the temperature, as shown in Fig. 4f–i, respectively.

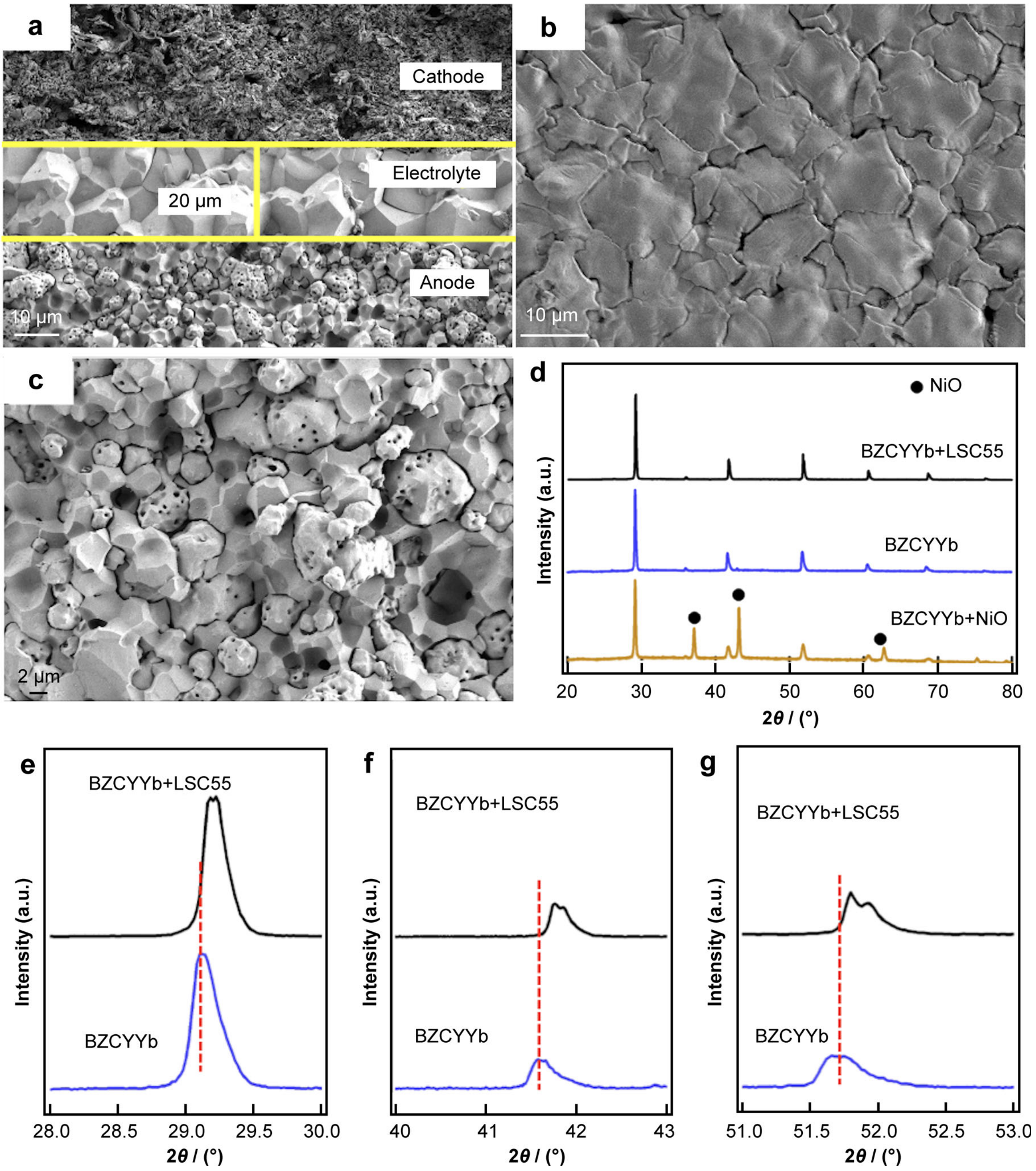

Fig. 2 SEM images of **a** cross section, **b** surface of electrolyte, and **c** anode for PCFC consisting of LSC82 cathode, BZCYYb electrolyte, CFL, and NiO-BZCYYb anode; **d** XRD patterns of anode, electrolyte, and electrolyte with sputtered CFL for PCFC; **e–g** enlarged XRD peaks of electrolyte and electrolyte with sputtered CFL

$$O_2(g) \rightarrow 2O_{TPB} \quad (1)$$

$$O_{TPB} + 2e^- \rightarrow O^{2-}_{TPB} \quad (2)$$

$$2H^+_{electrolyte} \rightarrow 2H^+_{TPB} \quad (3)$$

$$2H^+_{TPB} + O^{2-}_{TPB} \rightarrow H_2O_{TPB} \quad (4)$$

As shown in Fig. 4f, after applying the LSC55 CFL, the R_o decreased from 0.34 to 0.2 Ω·cm^2, 0.47 to 0.25 Ω·cm^2, 0.59 to 0.31 Ω·cm^2, 0.75 to 0.39 Ω·cm^2, and 0.95 to 0.5 Ω·cm^2, respectively. The corresponding proton conductivities increase from 0.0059 to 0.01 S·cm^{-1}, 0.004 to 0.008 S·cm^{-1}, 0.0033 to 0.006 S·cm^{-1}, 0.0027 to 0.005 S·cm^{-1}, and 0.002 to 0.004 S·cm^{-1} at 700, 650, 600, 550 and 500 °C, respectively. Even though the proton conductivities were lower than that recently report (0.028 S·cm^{-1} of BZCY442 at 700 °C) [43], the significant decreases in terms of R_o and proton conductivity strongly

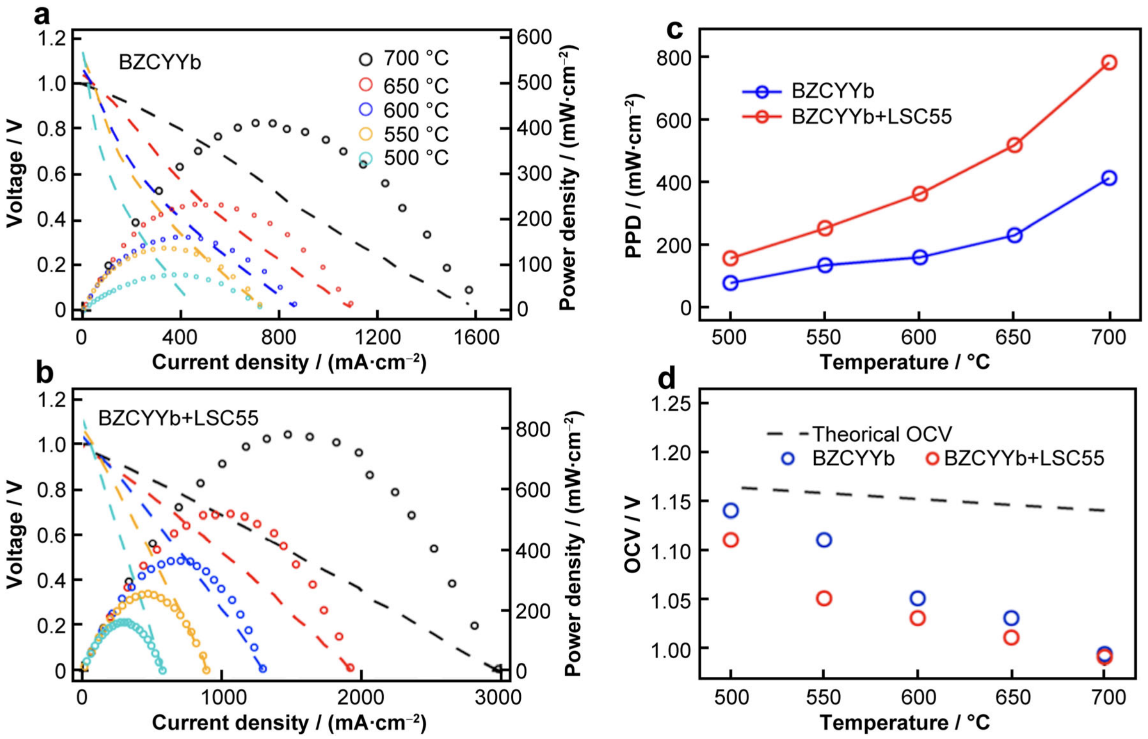

Fig. 3 *I*–*V* curves and corresponding power densities measured in temperature range of 500–700 °C for PCFCs **a** without and **b** with CFL (anode: wet hydrogen with 3% water (10 ml·min^{-1}); cathode: wet air (20 vol% O_2 and 80 vol% Ar, H_2O pressure of 2330 Pa; 30 ml·min^{-1}); **c** PPD as function of temperature; **d** comparison of theoretical and measured OCVs for two PCFCs

Table 1 A comparison of PPDs at 700 °C of PCFCs using similar Zr-rich BZCY(Yb) electrolyte and various air electrodes

Air electrodes	Electrolytes	PPDs / (mW·cm^{-2})	Refs.
LSC	BZCYYb	414	This work
LSC(CFL)	BZCYYb	783	This work
PBSCF	BZCYYb	1350 (650 °C)	[42]
BCFZY	BZCYYb	650	[5]
NBSCF	BZCYYb1711	1370	[41]
LSCF	BZCY442	381	[15]
BSCF	BZCY442	360	[37]
Pr_2NiO_4	BZCY442	234	[38]
BZCY-BSCFT	BZCY442	281	[39]
BSCF	BZCY442	360	[37]
BSCF	BZCY442	480	[40]

PBSCF: $Pr(Ba_{0.5}Sr_{0.5}Co_{1.5}Fe_{0.5})O_{5+\delta}$, BCFZY: $BaCe_{0.4}Fe_{0.4}Zr_{0.1}Y_{0.1}O_{3-\delta}$, NBSCF: $NdBa_{0.5}Sr_{0.5}Co_{1.5}Fe_{0.5}O_{5+\delta}$, LSCF: $La_{0.6}Sr_{0.4}Co_{0.2}Fe_{0.8}O_{3-\delta}$, BSCF: $Ba_{0.5}Sr_{0.5}Co_{0.2}Fe_{0.8}O_{3-\delta}$, BZCY-BSCFT: $Ba_{0.5}Sr_{0.5}(Co_{0.8}Fe_{0.2})_{0.9}Ti_{0.1}O_{3-\delta}$

suggests the improved proton conductivity in the PCFCs if using CFL.

On the other hand, the R_{p1} (Fig. 4g) and R_{p2} (Fig. 4h) of PCFCs with the CFL were smaller than those without the CFL. For example, R_{p1} and R_{p2} are sharply decreased from 0.55 to 0.11 Ω·cm^2 and from 0.58 to 0.32 Ω·cm^2 at 600 °C (R_{p1} and R_{p2} are decreased by 80% and 45% after using the CFL). These results indicate that the CFL can dramatically promote the proton incorporating process, as well as the surface diffusion or association desorption of oxygen species. Specifically, at a low temperature, e.g., 500 °C, the CFL also played an essential role in promoting mass transfer. At this temperature, the R_{p1} and R_{p2} decreased by 26% and 70%, respectively, indicating that the Reactions

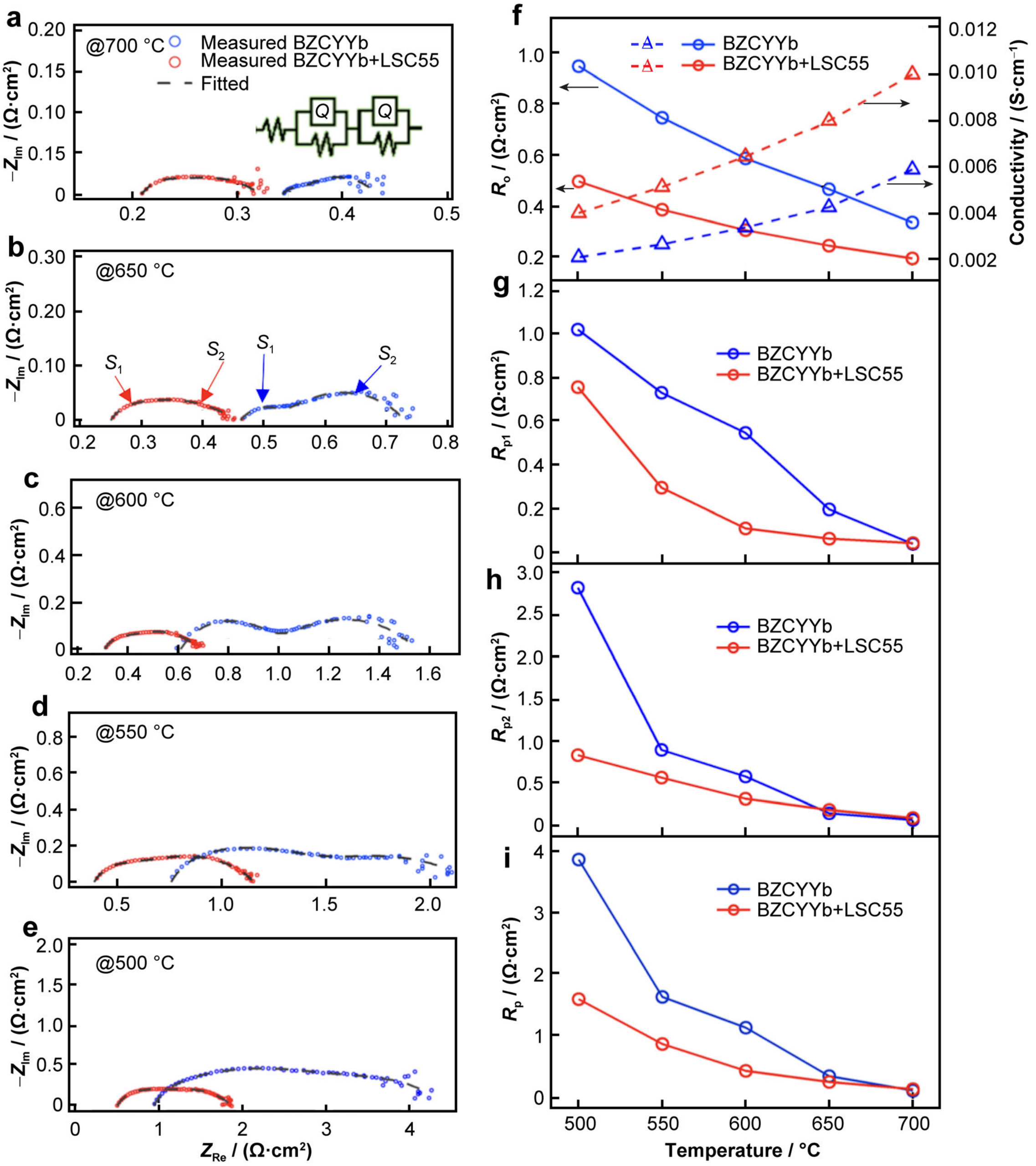

Fig. 4 Fitting results of EIS at **a** 700 °C, **b** 650 °C, **c** 600 °C, **d** 550 °C, and **e** 500 °C under OCV condition for comparison of PCFCs with and without CFL; **f** R_o and proton conductivity, **g** R_{p1}, **h** R_{p2}, and **i** R_p as function of temperatures for two PCFCs

(1, 2) may be the rate-determining step for the cell without the CFL. Furthermore, R_p is the sum of R_{p1} and R_{p2}, representing the total resistance of cathodic reaction. Reasonably, the obtained R_p values were 0.34, 1.13, 1.63, and 3.84 Ω·cm^2 for PCFCs without the CFL, while those for PCFCs with the CFL significantly decline to 0.25, 0.43, 0.86 and 1.59 Ω·cm^2 at 650, 600, 550 and 500 °C, respectively (Fig. 4i).

The Arrhenius plots of R_o^{-1} and R_p^{-1} for the PCFCs with and without the CFL were performed (Fig. 5). As shown in Fig. 5a, the activation energies (E_a) of R_o^{-1} were 0.29 and 0.32 eV for PCFCs with and without the CFL. The decreased E_a of R_o^{-1} for PCFC with CFL suggested that the CFL contributed greatly to the proton conduction of the PCFCs. On the other hand, the E_a of R_p^{-1} also greatly declined from 1.60 to 1.12 eV when the CFL was sputtered on the electrolyte (Fig. 5b). The dramatically decreased R_p indicated that the CFL can greatly promote hole/proton transfer, water formation and the surface kinetics of the cathode. This E_a value was lower than the widely used cathode materials, such as LSCF6428 (1.40 eV) [15], even comparable to that of the state-of-the-

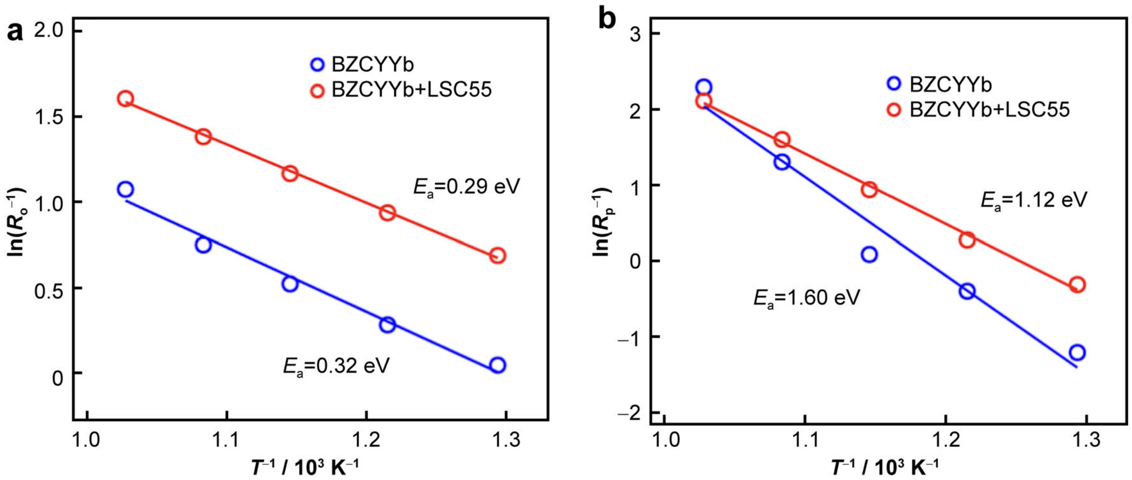

Fig. 5 **a** Arrhenius plots of R_o^{-1} and **b** R_p^{-1} for PCFCs with and without CFL from 500 to 700 °C

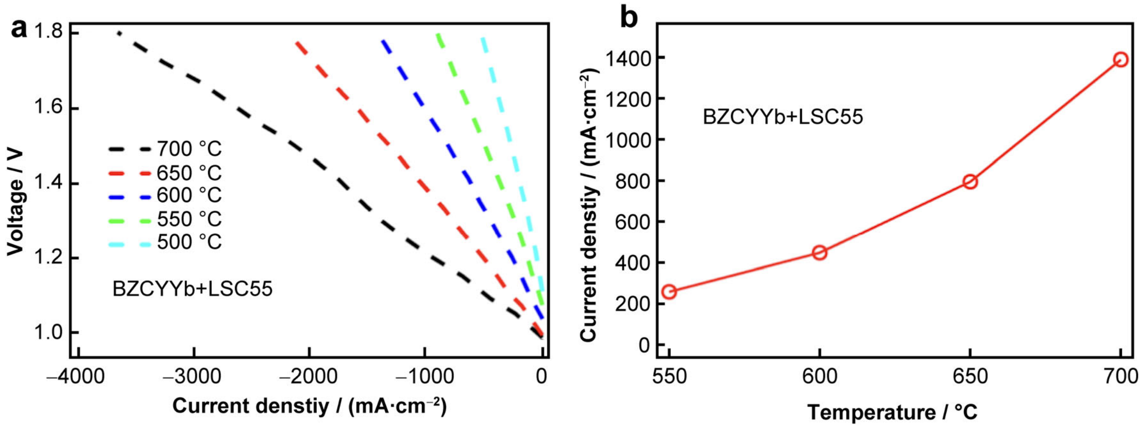

Fig. 6 *I–V* curves of PCFC with CFL operating in electrolysis mode at range of 500–700 °C with cathode of 30 ml·min^{-1} wet synthetic air, 20 vol% O_2 and 80 vol% Ar (H_2O pressure of 2330 Pa; 3% water partial pressure), and anode of 10 ml·min^{-1} humidified H_2 with 3% water

Table 2 Current densities at 1.3 V for protonic ceramic electrolysis cells based on BZCYYb electrolyte at 700 °C

Electrolytes	Anode	Current densities / (mA·cm^{-2})	Refs.
BZCYYb4411	LSC	1390	This work
BZCY442	SSC	30	[46]
BZCY532	SEFC-BZCY53	1000	[47]
BCZYZn53	LSCM-BCZYZn53	960	[48]
BCZYZn53	LSCM	22	[49]
BZY91	LSCF-BZY82	200	[50]

LSCM: $La_{0.75}Sr_{0.25}Cr_{0.5}Mn_{0.5}O_{3-\delta}$; BCZYZn53: $BaCe_{0.5}Zr_{0.3}Y_{0.16}Zn_{0.04}O_3$

art triple conducting $(La_{0.7}Sr_{0.3})(Mn_{0.7}Ni_{0.3})O_3$ (1.13 eV) [44].

In this work, we also preliminarily studied the application of the CFL strategy in protonic ceramic electrolysis cells (PCECs), which works under the reverse mode of fuel cell [45]. The *I–V* curves for PCECs with the CFL were recorded from 1.8 V to OCV at 500–700 °C, as shown in Fig. 6a. In detail, the current densities at 1.3 V were 1390, 706, 460 and 283 mA·cm^{-2} at 700, 650, 600 and 550 °C, respectively (Fig. 6b). Interestingly, the current density at 700 °C can reach 1390 mA·cm^{-2}, which was higher than that of the reported Zr-rich BZCY based electrolysis cells in the literatures (Table 2 [46–50]).

Based on the above results, the functional layer strategy proposed in this work plays an efficient role in promoting

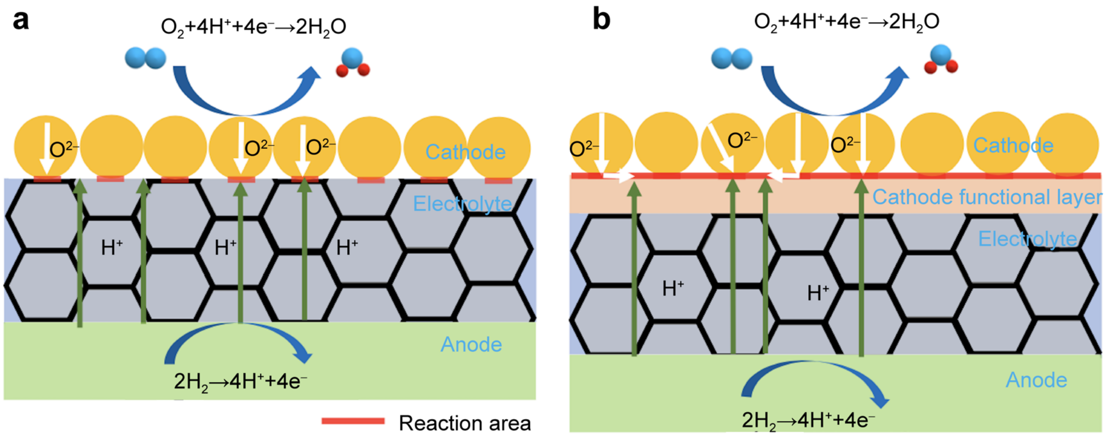

Fig. 7 Reaction mechanism of PCFCs with and without CFL

the electrochemical performance of PCFCs at intermediate temperatures. Both R_{o} and R_{p} were essentially lowered by using the CFL. For PCFCs, particularly those using a double e$^-$/O^{2-} conductor as cathode (like the LSC82 used in this work), the performance is significantly determined by the cathode−electrolyte−gas TPB. As shown in Fig. 7a, the proton transfers from the anode to the cathode side through electrolyte. Since the double e$^-$/O^{2-} conductor is not conductive for protons, the ORR can take place only on the electrolyte/cathode interface. In this regard, some protons cannot directly and immediately participate in the ORR, resulting in the slow kinetics at cathode. By contrast, once a functional LSC55 layer is applied (Fig. 7b), which was reported to be a proton−electron−oxide ion triple conducting phase [34], the O^{2-} and e$^-$ can transfer in the whole CFL. Therefore, the protons from the electrolyte can be directly reacted and form water as products. Reasonably, the reaction area is largely expanded to all the interface between the CFL and the electrolyte, thus resulting in the decreased R_{o} and R_{p} of PCFCs and improved power density.

4 Conclusion

In summary, $BaZr_{0.4}Ce_{0.4}Y_{0.1}Yb_{0.1}O_{3-\delta}$ electrolyte-based PCFCs with a sputtered ultra-thin CFL, i.e., ~ 90 nm $La_{0.5}Sr_{0.5}CoO_{3-\delta}$, was designed and successfully prepared. The PPD can reach 783 mW·cm^{-2} at 700 °C. At a lower temperature, e.g., 600 °C, the PPD increases by 2.24 times, and the ohmic and polarization resistance declines from 0.59 to 0.31 Ω·cm^2 and 1.12 to 0.43 Ω·cm^2, respectively, as compared with the PCFC without the CFL. The enhanced electrochemical performances are attributed to the functional layer between the electrolyte and the cathode, which plays the significant role in expanding the cathodic reaction area. We assume that if the CFL with rough surface where the cathode particles can be embedded inside, the electrochemical performance can be further improved, which is still pending in our group. These results indicate that the functional layer engineering strategy holds promise for the development of advanced PCFCs.

Acknowledgements This work was financially supported by China Post-doctoral Science Foundation (No. 2022M710856), Guangzhou Postdoctoral Research Project (No. 62104380), the Outstanding Youth Project of Natural Science Foundation of Guangdong Province (No. 2022B1515020020), the Funding by Science and Technology Projects in Guangzhou (Nos. 202206050003 and 202201010603) and Guangdong Engineering Technology Research Center for Hydrogen Energy and Fuel Cells.

Declarations

Conflict of interests The authors declare that they have no conflict of interest.

References

[1] Madhusudan C, Kasarapu V, Chittimadula M, Reddy YS, Reddy CV. Synthesis and characterization of Y and Dy co-doped ceria solid electrolytes for IT-SOFCs: a microwave sintering. Rare Met. 2021;40(11):3329. https://doi.org/10.1007/s12598-018-1059-1.

[2] Wang ZM, Feng XX, Xie ZX, Li YM. Preparation and characterization of $La_{1-x}Ba_xFeO_{3-\delta}$ cathode materials for intermediate-temperature solid oxide fuel cell. Chin J Rare Met. 2021; 45(10):1192. https://doi.org/10.13373/j.cnki.cjrm.xy19080033.

[3] Wang N, Tang CM, Du L, Zhu RJ, Xing LX, Song ZQ, Yuan BY, Zhao L, Aoki Y, Ye SY. Advanced cathode materials for protonic ceramic fuel cells: recent progress and future perspectives. Adv Energy Mater. 2022;12(34):2201882. https://doi.org/10.1002/aenm.202201882.

[4] Wang N, Yuan BY, Tang CM, Du L, Zhu RJ, Aoki Y, Wang W, Xing L, Ye S. Machine learning–accelerated development of efficient mixed protonic–electronic conducting oxides as the air electrodes for protonic ceramic cells. Adv Mate. 2022;34(51): 2203446. https://doi.org/10.1002/adma.202203446.

[5] Duan C, Tong J, Shang M, Nikodemski S, Sanders M, Ricote S, Almansoori A, O'Hayre R. Readily processed protonic ceramic

fuel cells with high performance at low temperatures. Science. 2015;349(6254):1321. https://doi.org/10.1126/science.aab3987.

[6] Pergolesi D, Fabbri E, D'Epifanio A, Di Bartolomeo E, Tebano A, Sanna S, Licoccia S, Balestrino G, Traversa E. High proton conduction in grain-boundary-free yttrium-doped barium zirconate films grown by pulsed laser deposition. Nat Mater. 2010;9(10):846. https://doi.org/10.1038/nmat2837.

[7] Ding XF, Shen JY, Gao XJ, Wang J. Enhanced electrochemical properties of $Sm_{0.2}Ce_{0.8}O_{1.9}$ film for SOFC electrolyte fabricated by pulsed laser deposition. Rare Metals. 2021;40(5):1294. https://doi.org/10.1007/s12598-014-0396-y.

[8] Choi S, Kucharczyk CJ, Liang Y, Zhang X, Takeuchi I, Ji HI, Haile SM. Exceptional power density and stability at intermediate temperatures in protonic ceramic fuel cells. Nat Energy. 2018;3(3):202. https://doi.org/10.1038/s41560-017-0085-9.

[9] An H, Lee HW, Kim BK, Son JW, Yoon KJ, Kim H, Shin D, Ji HI, Lee JH. A 5 × 5 cm^2 protonic ceramic fuel cell with a power density of 13 W cm^{-2} at 600 °C. Nat Energy. 2018;3(10):870. https://doi.org/10.1038/s41560-018-0230-0.

[10] Bae K, Kim DH, Choi HJ, Son JW, Shim JH. High-performance protonic ceramic fuel cells with 1 μm thick Y:Ba(Ce, Zr)O_3 electrolytes. Adv Energy Mater. 2018;8(25):1801315. https://doi.org/10.1002/aenm.201801315.

[11] Nien S, Hsu C, Chang C, Hwang B. Preparation of $BaZr_{0.1}Ce_{0.7}Y_{0.2}O_{3-\delta}$ based solid oxide fuel cells with anode functional layers by tape casting. Fuel Cells (Weinh). 2011;11(2):178. https://doi.org/10.1002/fuce.201000147.

[12] Nguyen NTQ, Yoon HH. Preparation and evaluation of $BaZr_{0.1}Ce_{0.7}Y_{0.1}Yb_{0.1}O_{3-\delta}$ (BZCYYb) electrolyte and BZCYYb--based solid oxide fuel cells. J Power Sources. 2013;231(213):218. https://doi.org/10.1016/j.jpowsour.2013.01.011.

[13] Choi SM, An H, Yoon KJ, Kim BK, Lee HW, Son JW, Kim H, Shin D, Ji HI, Lee JH. Electrochemical analysis of high-performance protonic ceramic fuel cells based on a columnar-structured thin electrolyte. Appl Energy. 2019;233:29. https://doi.org/10.1016/j.apenergy.2018.10.043.

[14] Bae K, Jang DY, Choi HJ, Kim D, Hong J, Kim BK, Lee JH, Son JW, Shim JH. Demonstrating the potential of yttrium-doped barium zirconate electrolyte for high-performance fuel cells. Nat Commun. 2017;8(1):14553. https://doi.org/10.1038/ncomms14553.

[15] Jeong S, Kobayashi T, Kuroda K, Kwon H, Zhu C, Habazaki H, Aoki Y. Evaluation of thin film fuel cells with Zr-rich $BaZr_xCe_{0.8-x}Y_{0.2}O_{3-\delta}$ electrolytes ($x \geq 0.4$) fabricated by a single-step reactive sintering method. RSC Adv. 2018;8(46):26309. https://doi.org/10.1039/C8RA04724C.

[16] Liu Y, Ran R, Tade MO, Shao Z. Structure, sinterability, chemical stability and conductivity of proton-conducting $BaZr_{0.6}M_{0.2}Y_{0.2}O_{3-\delta}$ electrolyte membranes: the effect of the M dopant. J Membr Sci. 2014;467:100. https://doi.org/10.1016/j.memsci.2014.05.020.

[17] Yang L, Zuo C, Wang S, Cheng Z, Liu M. A novel composite cathode for low-temperature SOFCs based on oxide proton conductors. Adv Mater. 2008;20(17):3280. https://doi.org/10.1002/adma.200702762.

[18] Yang L, Liu Z, Wang S, Choi Y, Zuo C, Liu M. A mixed proton, oxygen ion, and electron conducting cathode for SOFCs based on oxide proton conductors. J Power Sources. 2010;195(2):471. https://doi.org/10.1016/j.jpowsour.2009.07.057.

[19] Choi J, Kim B, Song SH, Park JS. A composite cathode with undoped $LaFeO_3$ for protonic ceramic fuel cells. Int J Hydrog. 2016;41(22):9619. https://doi.org/10.1016/j.ijhydene.2016.03.115.

[20] Dailly J, Taillades G, Ancelin M, Pers P, Marrony M. High performing $BaCe_{0.8}Zr_{0.1}Y_{0.1}O_{3-\delta}$-$Sm_{0.5}Sr_{0.5}CoO_{3-\delta}$ based protonic ceramic fuel cell. J Power Sources. 2017;361:221. https://doi.org/10.1016/j.jpowsour.2017.06.089.

[21] Lee S, Park S, Wee S, Baek HW, Shin D. One-dimensional structured $La_{0.6}Sr_{0.4}Co_{0.2}Fe_{0.8}O_{3-\delta}$-$BaCe_{0.5}Zr_{0.35}Y_{0.15}O_{3-\delta}$ composite cathode for protonic ceramic fuel cells. Solid State Ion. 2018;320:347. https://doi.org/10.1016/j.ssi.2018.03.010.

[22] Song YF, Chen YB, Wang W, Zhou C, Zhong YJ, Yang GM, Zhou W, Liu ML, Shao ZP. Self-assembled triple-conducting nanocomposite as a superior protonic ceramic fuel cell cathode. Joule. 2019;3(11):2842. https://doi.org/10.1016/j.joule.2019.07.004.

[23] Zhao Z, Cui J, Zou M, Mu S, Huang H, Meng Y, He K, Brinkman KS, Tong J. Novel twin-perovskite nanocomposite of Ba–Ce–Fe–Co–O as a promising triple conducting cathode material for protonic ceramic fuel cells. J Power Sources. 2020;450:227609. https://doi.org/10.1016/j.jpowsour.2019.227609.

[24] Wang N, Toriumi H, Sato Y, Tang C, Nakamura T, Amezawa K, Kitano S, Habazaki H, Aoki Y. $La_{0.8}Sr_{0.2}Co_{1-x}Ni_xO_{3-\delta}$ as the efficient triple conductor air electrode for protonic ceramic cells. ACS Appl Energy Mater. 2020;4(1):554. https://doi.org/10.1021/acsaem.0c02447.

[25] Zohourian R, Merkle R, Raimondi G, Maier J. Mixed-conducting perovskites as cathode materials for protonic ceramic fuel cells: understanding the trends in proton uptake. Adv Funct Mater. 2018;28(35):1801241. https://doi.org/10.1002/adfm.201801241.

[26] Ren R, Wang Z, Xu C, Sun W, Qiao J, Rooney DW, Sun K. Tuning the defects of the triple conducting oxide $BaCo_{0.4}Fe_{0.4}Zr_{0.1}Y_{0.1}O_{3-\delta}$ perovskite toward enhanced cathode activity of protonic ceramic fuel cells. J Mater Chem A. 2019;7(31):18365. https://doi.org/10.1039/C9TA04335G.

[27] Zohourian R, Merkle R, Maier J. Proton uptake into the protonic cathode material $BaCo_{0.4}Fe_{0.4}Zr_{0.2}O_{3-\delta}$ and comparison to protonic electrolyte materials. Solide State Ion. 2017;299:64. https://doi.org/10.1016/j.ssi.2016.09.012.

[28] Wang N, Hinokuma S, Ina T, Toriumi H, Katayama M, Inada Y, Zhu C, Habazaki H, Aoki Y. Incorporation of bulk proton carriers in cubic perovskite manganite driven by interplays of oxygen and manganese redox. Chem Mater. 2019;31(20):8383. https://doi.org/10.1021/acs.chemmater.9b02131.

[29] Aoki Y, Tsuji E, Motohashi T, Kowalski D, Habazaki H. $La_{0.7}Sr_{0.3}Mn_{1-x}Ni_xO_{3-\delta}$ electrocatalysts for the four-electron oxygen reduction reaction in concentrated alkaline media. J Phys Chem C. 2018;122(39):22301. https://doi.org/10.1021/acs.jpcc.8b06741.

[30] Zhou Y, Zhang W, Kane N, Luo Z, Pei K, Sasaki K, Choi Y, Chen Y, Ding D, Liu M. An efficient bifunctional air electrode for reversible protonic Ceramic electrochemical cells. Adv Funct Mater. 2021;31(40):2105386. https://doi.org/10.1002/adfm.202105386.

[31] Zhou Y, Liu E, Chen Y, Liu Y, Zhang L, Zhang W, Luo Z, Kane N, Zhao B, Soule L, Niu Y, Ding Y, Ding H, Ding D, Liu M. An active and robust air electrode for reversible protonic ceramic electrochemical cells. ACS Energy Lett. 2021;6(4):1511. https://doi.org/10.1021/acsenergylett.1c00432.

[32] Liu B, Jia L, Chi B, Pu J, Li J. A novel $PrBaCo_2O_{5+\sigma}$-$BaZr_{0.1}Ce_{0.7}Y_{0.1}Yb_{0.1}O_3$ composite cathode for proton-conducting solid oxide fuel cells. Compos B Eng. 2020;191:107936. https://doi.org/10.1016/j.compositesb.2020.107936.

[33] Li W, Guan B, Ma L, Hu S, Zhang N, Liu X. High performing triple-conductive $Pr_2NiO_{4+\delta}$ anode for proton-conducting steam solid oxide electrolysis cell. J Mater Chem A. 2018;6(37):18057. https://doi.org/10.1039/c8ta04018d.

[34] Tang C, Akimoto K, Wang N, Fadillah L, Kitano S, Habazaki H, Aoki Y. The effect of an anode functional layer on the steam electrolysis performances of protonic solid oxide cells. J Mater

Chem A. 2021;9(24):14032. https://doi.org/10.1039/d1ta02848k.

[35] Shimada H, Yamaguchi Y, Ryuma MM, Sumi H, Nomura K, Shin W, Mikami Y, Yamauchi K, Nakata Y, Kuroha T, Mori M, Mizutani Y. Protonic ceramic fuel cell with Bi-layered structure of $BaZr_{0.1}Ce_{0.7}Y_{0.1}Yb_{0.1}O_{3-\delta}$ functional interlayer and $BaZr_{0.8}Yb_{0.2}O_{3-\delta}$ electrolyte. J Electrochem Soc. 2021;168(12):124504. https://doi.org/10.1149/1945-7111/ac3d04.

[36] Shimada H, Yamaguchi T, Sumi H, Nomura K, Yamaguchi Y, Fujishiro Y. Improved transport property of proton-conducting solid oxide fuel cell with multi-layered electrolyte structure. J Power Sources. 2017;364:458. https://doi.org/10.1016/j.jpowsour.2017.08.038.

[37] Liu Y, Guo Y, Ran R, Shao Z. A novel approach for substantially improving the sinterability of $BaZr_{0.4}Ce_{0.4}Y_{0.2}O_{3-\delta}$ electrolyte for fuel cells by impregnating the green membrane with zinc nitrate as a sintering aid. J Membr Sci. 2013;437:189. https://doi.org/10.1016/j.memsci.2013.03.002.

[38] Nasani N, Ramasamy D, Mikhalev S, Kovalevsky AV, Fagg DP. Fabrication and electrochemical performance of a stable, anode supported thin $BaCe_{0.4}Zr_{0.4}Y_{0.2}O_{3-\delta}$ electrolyte protonic ceramic fuel cell. J Power Sources. 2015;278:582. https://doi.org/10.1016/j.jpowsour.2014.12.124.

[39] Bi L, Fabbri E, Traversa E. Effect of anode functional layer on the performance of proton-conducting solid oxide fuel cells (SOFCs). Electrochem commun. 2012;16(1):37. https://doi.org/10.1016/j.elecom.2011.12.023.

[40] Guo Y, Lin Y, Ran R, Shao Z. Zirconium doping effect on the performance of proton-conducting $BaZr_yCe_{0.8-y}Y_{0.2}O_{3-\delta}$ ($0.0 \leq y \leq 0.8$) for fuel cell applications. J Power Sources. 2009;193(2):400. https://doi.org/10.1016/j.jpowsour.2009.03.044.

[41] Kim J, Sengodan S, Kwon G, Ding D, Shin J, Liu M, Kim G. Triple-conducting layered perovskites as cathode materials for proton-conducting solid oxide fuel cells. ChemSusChem. 2014;7(10):2811. https://doi.org/10.1002/cssc.201402351.

[42] Choi S, Davenport T, Haile S. Protonic ceramic electrochemical cells for hydrogen production and electricity generation: exceptional reversibility, stability, and demonstrated faradaic efficiency. Energy Environ Sci. 2019;12:206. https://doi.org/10.1039/c8ee02865f.

[43] Han D, Liu X, Bjoheim T, Uda T. Yttrium-doped barium zirconate-cerate solid solution as proton conducting electrolyte: why higher cerium concentration leads to better performance for fuel cells and electrolysis cells. Adv Energy Mater. 2021;11:2003149. https://doi.org/10.1002/aenm.202003149.

[44] Wang N, Hinokuma S, Ina T, Zhu C, Habazaki H, Aoki Y. Mixed proton–electron–oxide ion triple conducting manganite as an efficient cobalt-free cathode for protonic ceramic fuel cells. J Mater Chem A. 2020;8(21):11041. https://doi.org/10.1039/d0ta03899g.

[45] Duan C, Kee R, Zhu H, Sullivan N, Zhu L, Bian L, Jennings D, O'Hayre R. Highly efficient reversible protonic ceramic electrochemical cells for power generation and fuel production. Nat Energy. 2019;4(3):230. https://doi.org/10.1038/s41560-019-0333-2.

[46] Kobayashi T, Kuroda K, Jeong S, Kwon H, Zhu C, Habazaki H, Aoki Y. Analysis of the anode reaction of solid oxide electrolyzer cells with $BaZr_{0.4}Ce_{0.4}Y_{0.2}O_{3-\delta}$ electrolytes and $Sm_{0.5}Sr_{0.5}CoO_{3-\delta}$ anodes. J Electrochem Soc. 2018;165(5):F342. https://doi.org/10.1149/2.0891805jes.

[47] Huan D, Shi N, Zhang L, Tan W, Xie Y, Wang W, Xia C, Peng R, Lu Y. New, efficient, reliable air electrode material for proton-conducting reversible solid oxide cells. ACS Appl Mater Inter. 2018;10(2):1761. https://doi.org/10.1021/acsami.7b16703.

[48] Gan Y, Zhang J, Li Y, Li S, Xie K, Irvine JTS. Composite oxygen electrode based on LSCM for steam electrolysis in a proton conducting solid oxide electrolyzer. J Electrochem Soc. 2012;159(11):F763. https://doi.org/10.1149/2.018212jes.

[49] Gan L, Ye L, Liu M, Tao S, Xie K. A scandium-doped manganate anode for a proton-conducting solid oxide steam electrolyzer. RSC Adv. 2016;6(1):641. https://doi.org/10.1039/C5RA19844E.

[50] Bi L, Shafi SP, Traversa E. Y-doped $BaZrO_3$ as a chemically stable electrolyte for proton-conducting solid oxide electrolysis cells (SOECs). J Mater Chem A. 2015;3(11):5813. https://doi.org/10.1039/C4TA07202B.